

Polarization Dependent Light-Driven Liquid Crystal Elastomer Actuators Based on Photothermal Effect

Yong Li, Yanjun Liu, and Dan Luo*

Light-driven liquid crystal elastomers (LCEs) have drawn a great deal of attention as one kind of the most attractive and exciting soft active materials because of their wide application in biomimetic devices, artificial muscles, sensors, and soft robotics. Recently, photothermal effect based LCE actuators have emerged as a promising material with features of biocompatibility, high tissue penetration ability, and the ease and flexibility in materials design. However, to achieve polarized light-driven LCE actuators, where the polarization can serve as an additional manipulation degree of freedom for actuators manipulation, is still a challenge. Herein, a strategy of constructing a linearly polarization dependent light-driven soft actuator based on dichroic dye (DD) doped LCEs is demonstrated. Three polarization-dependent photothermal effect based LCE actuators, including oscillators, bionic dog swinging tail, and light-mill are experimentally investigated for the first time. The polarization of light is proved to perform as controlling parameter and provides an additional degree of freedom to photothermal effect based light-driven LCE actuators besides the wavelength and intensity of light. The DD-doped LCE actuator with good polarization dependence shows great potential applications in soft robotics and biomimetic field.

Soft actuators have drawn a great deal of attention as one kind of the most attractive and exciting soft active materials because of their widely application in biomimetic devices, artificial muscles, sensors, and soft robotics.^[1] Various stimuli, such as temperature, light, and electric field,^[2] have been applied to realize the deformation or motion of soft actuators. Among them, photoresponsive liquid crystal elastomers (LCEs, including liquid crystal polymer networks) have emerged as a promising material system due to their advantageous features, such as remotely, instantly, precisely control without the aid of batteries, electric wires, and contact-based driving system.^[3] One effective


strategy to fabricate photoresponsive LCEs is using azobenzene derivative/monomer doped polymer with reversible trans-cis photoisomerization based on photochemical effect.^[4] Another approach is based on simply doping photothermal agents into LCE matrices, where the actuation can be realized through LC-to-isotropic phase transition by light induced photothermal effect.^[5] Several materials, such as carbon nanotubes (CNTs),^[6] gold nanorods (AuNRs),^[7] graphene oxide (GO),^[8] organic dyes,^[9] and polydopamine,^[10] have been used as the thermal agents for photoresponsive actuator in widely application of solar energy harvesting device,^[6e] oscillator,^[8c,9d] flytrap,^[9e] caterpillar,^[6b,9f,g] flower,^[6f] and soft robotics.^[6c,d,7b,c,9b,c,j,10a,b]

Currently, the reported photothermal effect based LCE actuators are mainly modulated by optical parameters of wavelength^[9a,b,e,g,10c,11] or intensity.^[9f,h,i,12] In wavelength based modulation, artificial flytrap and caterpillar-inspired inching robot through doping photothermal material of dispersed red 1 have been demonstrated by visible light-driven LCE actuators.^[9e,g] Near infrared (NIR) light driven LCEs doped with IR-absorbing dye have been applied in soft actuators with radial/azimuthal alignment layer and ultrafast photoresponsive speed,^[9a,b] and oscillator,^[10c] respectively. Visible and infrared three-wavelength modulated actuators have been reported as multidirectional walker robot as well.^[11] In intensity based modulation, caterpillar locomotion has been realized by light-driven soft robot through laser beam scanning both in visible and near infrared light.^[9f,h,12] Structure light-driven biomimetic swimming and versatile locomotion of photoresponsive soft microrobots based on photothermal effect has been reported.^[9i] However, to achieve polarization driven LCE actuators, where the polarization can serve as an additional degree of freedom (DOF) for soft actuator manipulation, is still a challenge in photothermal effect based LCE actuators due to the poor polarization absorption property in previously used photothermal agents. Lacking of polarization modulation will limit the shape morphing modes of actuators and weaken the manipulation capability of light. Therefore, it is highly desirable to develop a new strategy to fabricate LCE actuators such that the polarization of light can be used as a modulation parameter.

Herein, we demonstrate a strategy of constructing a linearly polarization light-driven LCE soft actuator that can address the

Dr. Y. Li, Prof. Y. Liu, Prof. D. Luo
Department of Electrical & Electronic Engineering
Southern University of Science and Technology
Xueyuan Road 1088, Nanshan District, Shenzhen, Guangdong 518055, China
E-mail: luod@sustech.edu.cn

Dr. Y. Liu
College of Physics and Optoelectronic Engineering
Shenzhen University
Shenzhen 518060, China

 The ORCID identification number(s) for the author(s) of this article can be found under <https://doi.org/10.1002/adom.202001861>.

DOI: 10.1002/adom.202001861

above challenge. To the best of our knowledge, polarization dependent LCE actuators based on photothermal effect have been demonstrated for the first time. This strategy is based on doping dichroic dye (DD) into LCEs, where the polarized absorption of DD modulates soft actuator through linearly polarization of light while the photothermal conversion of DD transforms optical energy into heating. The polarization dependent properties of DD doped LCE films are characterized at visible light in wavelength of 488 nm. Polarization of light, as an optical parameter, is used for tuning the oscillation frequency instead of intensity. Three polarization-dependent LCE actuators, including oscillators, bionic dog swinging tail, and light-mill are fabricated. The polarization of light is experimentally demonstrated to perform controlling parameter and provide an additional DOF to photothermal effect based light-driven LCE actuators besides the wavelength and intensity of light.

Chemical structures of reactive mesogen (RM) monomers RM257 and RM 006, dichroic dye RL002, and photoinitiator Irgacure 651 are shown in Figure 1a. The absorption spectra of dichroic dye RL002 is demonstrated in Figure 1b, where α is the angle between the polarization direction of the linearly polarized incident light (L) and the orientation of dichroic dye (D).

The red and blue curve represents the absorbance of dichroic dye for $\alpha = 0^\circ$ ($L//D$) and $\alpha = 90^\circ$ ($L \perp D$) in range of 300–800 nm, respectively. It is seen that the absorbance of dichroic dye RL002 in case of $\alpha = 0^\circ$ (absorbance of 2.5) is ≈ 3.4 times of that in case of $\alpha = 90^\circ$ (absorbance of 0.75) at 488 nm. The absorbance contrast of dichroic dye RL002 indicates the polarization-dependent tuning feasibility of DD-doped LCE actuator by light with linearly polarization at wavelength of 488 nm. Figure 1c depicts the schematic illustration of linearly polarized light and LCE film with splay orientation. In LCE film, the reactive mesogens (blue rod) and dichroic dye molecules (red rod) self-assemble to a splay configuration due to the vertical alignment (VA) and parallel alignment (PA) in VA surface (top) and PA surface (bottom), respectively (Figure S1, Supporting Information). An LCE film with size of $0.2 \text{ cm} \times 1 \text{ cm}$ was cut from the prepared film (Figure S2, Supporting Information) and denoted as Sample 1, where the long side direction (x axis) was parallel to the alignment direction of RMs on PA surface (M). During light illumination, the local temperature of LCE film increases due to the photothermal conversion of dichroic dye. When the LCE film is heated beyond the LC-isotropic phase transition temperature, the orientation of LC mesogens changes to randomly alignment, leading to extension on VA

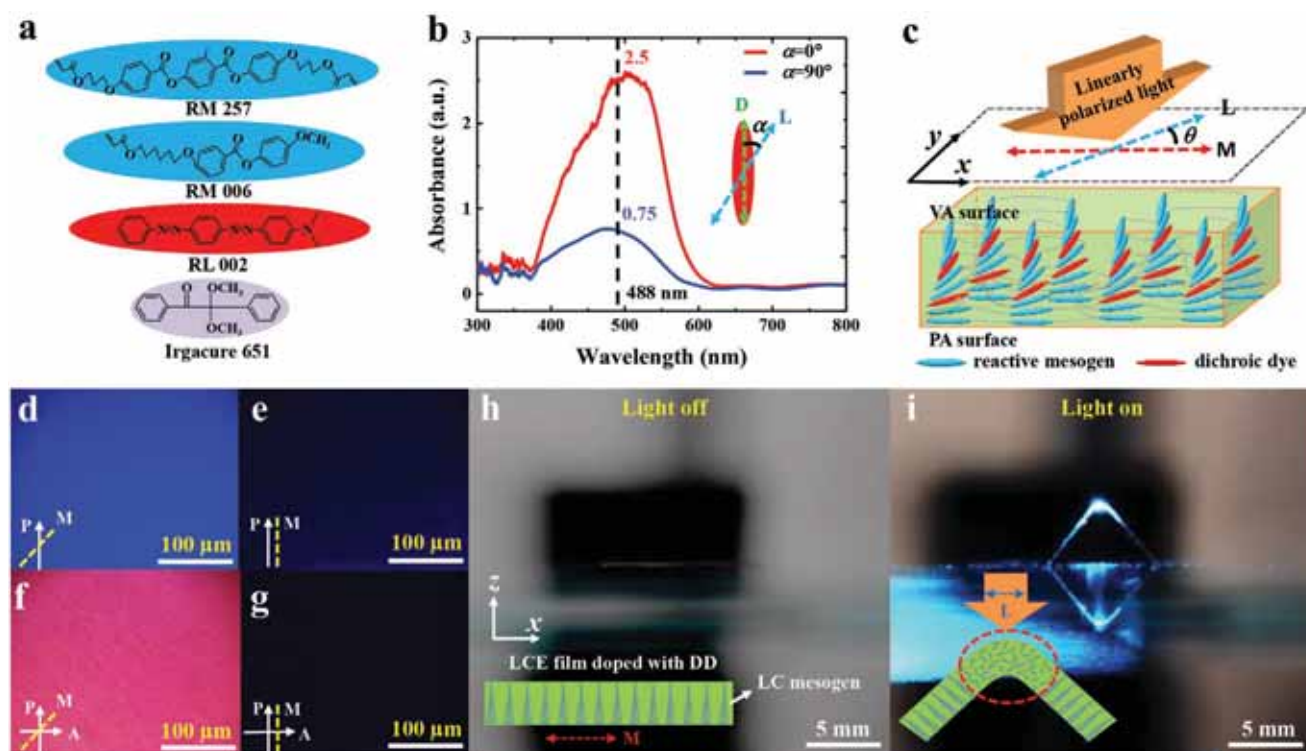


Figure 1. Polarization light driven bending based on photothermal effect. a) Chemical structures of components to form liquid crystals elastomers. b) Absorption spectra of the dichroic dye. α is the angle between the polarization direction of linearly polarized light (L) and orientation of dichroic dye (D). Red and blue curve represents the absorbance of dichroic dye for $\alpha = 0^\circ$ (L is parallel to D) and $\alpha = 90^\circ$ (L is perpendicular to D) in range of 300–800 nm, respectively. c) Schematic illustration of LCE film with splay orientation and linearly polarized incident light. VA surface (top) and PA surface (bottom) represents the vertical alignment (VA) and parallel alignment (PA) surface in LCE film. M is the orientation direction of LC mesogens on PA surface. θ is the angle between L and M . The optical images of DD doped LCE film observed under POM at 488 nm without analyzer, where the angle between polarizer (P) and M is d) 45° and e) 0° , respectively. The optical images of DD doped LCE film observed under POM at 488 nm with analyzer, where the angle between polarizer (P) and M is f) 45° and g) 0° , respectively. The LCE film actuator in cases of h) light off and i) light on. The L is parallel to the M . The cross sectional schematic illustration of LCE film doped with DD is demonstrated, where the orientation of LC mesogen is depicted. The irradiation region by light is shown by the red circle, where the LC mesogen is randomly orientated in isotropic phase due to photothermal effect.

surface and contraction on PA surface and finally bending action towards the PA surface. When the LCE film is cooled into the LC phase, the LC mesogens return to the original orientation and the LCE film recovers to its original state. For polarization light driven LCE actuator, the angle between the polarization direction of linearly polarized light (L) and orientation direction of LC mesogens (M , along x axis) on PA surface in LCE film is represented by θ , which directly determines the light absorption of dichroic dye (aligning with the LC mesogens). The photothermal effect is maximum and minimum at $\theta = 0^\circ$ and $\theta = 90^\circ$, resulting in the largest and smallest bending angle of LCE film, respectively.

Figure 1d,e shows the optical images of LCE film under the polarization optical microscope (POM) with only polarizer but not analyzer, where the white arrow and yellow dashed-line represents the polarization direction of polarizer (P) and the orientation direction of LC mesogens on PA surface (M), respectively. Figure 1f,g shows the POM images of LCE film with both polarizer and analyzer, where the polarization direction of analyzer is represented by A . It is seen that the color of LCE film changes from bright (blue or red) to dark when the angle between M and P varies from 45° (Figure 1d,f) to 0° (Figure 1e,g), which indicates the dichroic dye molecules are well aligned by the LC mesogens in splay configuration of LCE film due to a good host-guest interaction. The optical setup of the polarization light driven system consisted of an argon-ion laser with wavelength of 488 nm (Coherent Inc.), a polarizer and a half-wave plate at 488 nm (all from Thorlabs). The polarization direction L of laser light was controlled by rotating the half-wave plate that only changes the polarization direction without intensity variation. The output laser light was then focused on the LCE film by a convex lens. Figure 1h,i shows the photograph of the DD doped LCE film on surface of a silica glass when light was off and on, respectively. The schematic illustration of LCE film with orientation of LC mesogens in cross section is also depicted, where the M is along the horizontal direction and the polarization direction of light L is set to be parallel to M . When the light was on, the light energy absorbed by dichroic dye was converted into heat energy and the LCE phase transition was excited afterwards. Therefore, the LCE film was bending at the region irradiated by the light, finally resulting in the standing up of LCE film (Video S1, Supporting Information). The region irradiated by light is shown by red circled, where the orientation of LC mesogens is random due to the photothermal effect (Figure 1i).

Due to the polarization dependent absorption property of dichroic dye, the dichroic dye doped LCE actuator can be driven by the linearly polarized light, and the polarization direction of linearly polarized light can be used as a tuning parameter to control the action of actuator. Figure 2a demonstrates the bending of LCE film actuator under different polarizations of irradiation light (488 nm) with fixed intensity of 20 mW cm^{-2} . In our experiment, one end of a LCE film actuator (Sample 1) with size of $0.2 \text{ cm} \times 1 \text{ cm}$ was fixed by a tweezer. The schematic illustration of LC mesogens orientation in cross section of LCE film and polarization direction of light is shown inset, and β represents the bending angle of LCE actuator from original position to bending position under light irradiation. Here, the laser light irradiated from bottom (VA surface) to up (PA

surface) direction, leading to upwards bending action. It is seen that, the bending angle β is maximal (138°) in the case of $\theta = 0^\circ$ ($L//M$), indicating the largest photothermal conversion. With the increase of angle θ from 0° up to 90° ($L \perp M$), the bending angle β decreases gradually and finally reaches the minimal value of 51° , which corresponds to the smallest photothermal conversion. The polarization dependent bending of LCE film actuator is shown in Video S2 in the Supporting Information. Figure 2b plots the curves of bending angle (red triangles) and temperature (blue squares) versus laser power density at fixed angle $\theta = 0^\circ$. The bending angle β starts to increase from 0° to 138° as the laser power density increases from threshold of $8\text{--}26 \text{ mW cm}^{-2}$, corresponding to linearly increase of temperature from 28.1 to 58.1°C . The temperature threshold is around 37.5°C . Figure 2c plots the relationship of bending angle versus the θ at laser power density of 20 mW cm^{-2} . The bending angle decreases from 138° to 51° when the angle θ varies from 0° to 90° . The difference of bending angle $\beta_{\theta=0^\circ}$ and $\beta_{\theta=90^\circ}$ versus laser power density at fixed angle $\theta = 0^\circ$ is plotted in Figure 2d. The angle difference $\beta_{\theta=0^\circ} - \beta_{\theta=90^\circ}$ starts from 0° (beyond the threshold of 8 mW cm^{-2}) and increases to the maximum of 87° at 20 mW cm^{-2} as the increase of laser power density. Then it decreases to 31° when the laser power density further increases to 26 mW cm^{-2} . The IR thermal images of LCE are shown in the Figure S3 in the Supporting Information. In Figure S3 (Supporting Information), there is a spot on the LCE tape with a diameter of about 2 mm, where the temperature of irradiation area increases from 39.9 to 50.9°C as the angle θ changes from 90° to 0° .

Figure 2e depicts temperature (red curve) and transmittance (blue curve) of LCE film actuator as functions on different angle θ , where the laser power density is 20 mW cm^{-2} . In the irradiation region, the temperature is decreased from 50.5 to 40.2°C when θ increases from 0° to 90° . The temperature was recorded by a thermal imager. The transmittance increases from 0.49% to 18.13% with increasing of angle θ from 0° to 90° , the transmittance at $\theta = 90^\circ$ is 36.9 times higher than that at $\theta = 0^\circ$. The increasing transmittance as the increase of angle θ indicates a slowly decrease in the photothermal conversion efficiency, which is caused by the decreased absorption ability of the dichroic dye when the polarization direction of light rotates from parallel to perpendicular to the long axis of dichroic dye molecules. Figure S4 in the Supporting Information shows the relationship of bending angle versus time as the angle θ is switched between 0° and 90° , which was measured by an oscilloscope. The rise time and decay time was measured to be 0.11 and 0.16 s when the θ was switched from 0° to 90° (β was increased from 51° to 138°) and back, respectively. To the best of our knowledge, the bending angle difference of 87° and the response time of 0.11 s are currently the best in the field of polarized light-driven LCE actuators; however, our oscillator is slower than the fast actuator with response time of 5 ms by combining CNTs and vanadium dioxide (VO_2).^[6b] It is noticed that, the polarization-dependent LCE actuator can be extended to other visible wavelengths such as green, red, and near infrared light with properly selection of DD with corresponding absorption spectrum.

The same LCE film (Sample 1) was then used as an oscillator that was fixed by a tweezer vertically as shown in Figure 3a. The

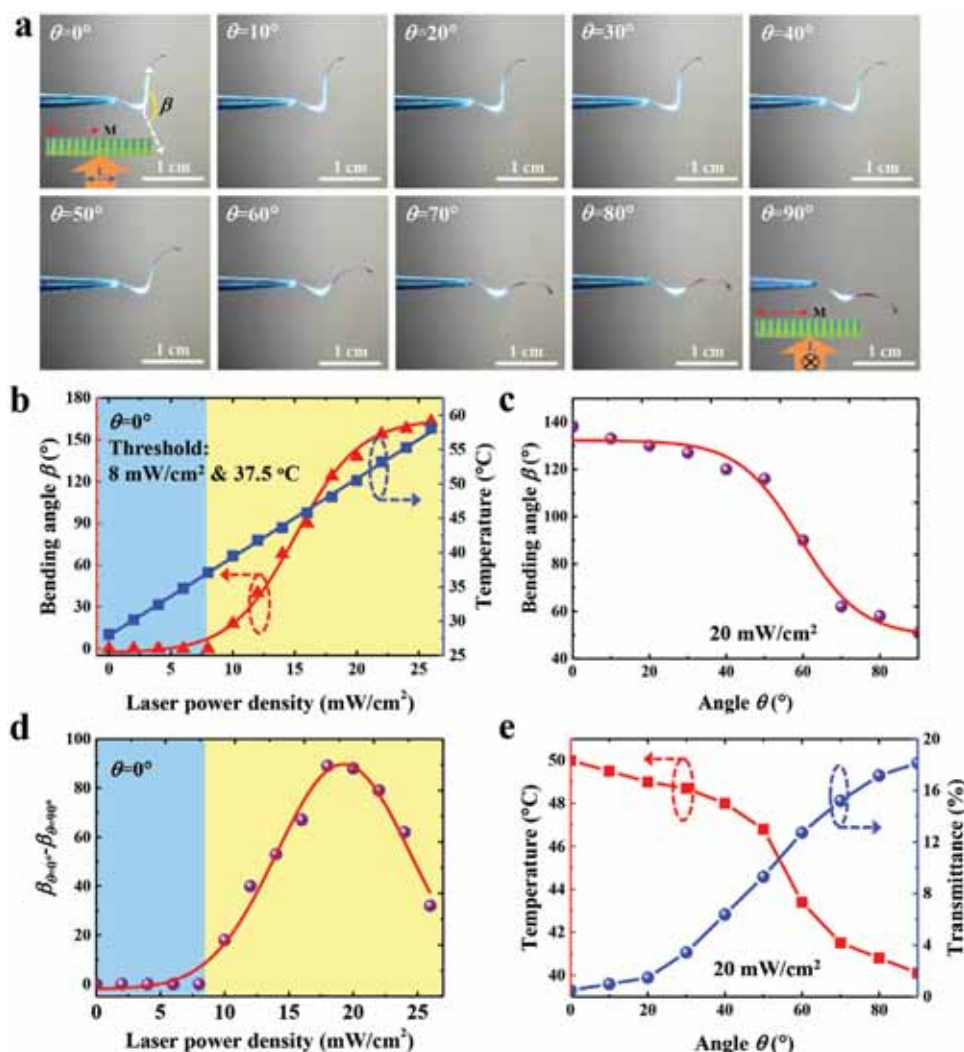


Figure 2. Polarization dependent properties of LCE film actuator. a) Photos depicting LCE film actuator bending at different polarized light illumination, where the θ varies from 0° to 90° and the laser light travels from bottom to up. The cross sectional schematic illustration of LCE film is demonstrated. The direction of L is parallel and perpendicular to M in case of $\theta = 0^\circ$ and $\theta = 90^\circ$, respectively. b) Curves of bending angle (red triangles) and temperature (blue squares) versus laser power density at fixed angle $\theta = 0^\circ$. c) Relationship of bending angle versus the θ at laser power density of 20 mW cm^{-2} . d) The difference of bending angle $\beta_{\theta=0^\circ}$ and $\beta_{\theta=90^\circ}$ versus laser power density at fixed angle $\theta = 0^\circ$. e) Temperature (red curve) and transmittance (blue curve) of LCE film actuator as functions on different angle θ , where the laser power density is 20 mW/cm^2 .

schematic illustration of LC mesogens orientation in cross section of LCE film is shown inset. Herein, the laser light irradiated from left (VA surface) to right (PA surface) direction. The laser polarization direction was set to be parallel to the alignment direction of LC on PA surface ($L//M$), meaning $\theta = 0^\circ$. When there was no laser irradiation (0 mW cm^{-2}), the LCE film actuator was vertical. As the laser power density increased up to 26 mW cm^{-2} , the LCE film actuator would bend up to $\beta = 105^\circ$ but without oscillation (Figure 3b). The LCE film started to oscillate when the laser power density exceeded the threshold of 26 mW cm^{-2} . Figure 3c demonstrates the oscillation of LCE film under laser power density of 39 mW cm^{-2} . The oscillation mechanism is that: First, the absorption ability of the DD became weaker when the DD molecules were rotated with the bending of LCE film in the irradiation region, which was due to the increased angle between the alignment direction of DD and

the polarization direction of laser. Then, the weaker absorption ability of the DD resulted in a decrease of the temperature in the irradiation region of LCE film, accompanied with the reorientation of LC from isotropic to LC phase, leading to decrease of bending angle β . Finally, both the bending angle β and the temperature of the LCE film in the irradiation region increased again. The repeated decrease and increase of the bending angle β led to the formation of oscillation. The deflection angle of the oscillator can be calculated according to $\Delta\beta = \beta_1 - \beta_0$, where β_1 is the maximal bending angle, and β_0 is the initial bending angle in the oscillation procedure. Figure 3d depicts the deflection angle $\Delta\beta$ (red curve) and oscillation frequency (blue curve) as function on laser power density at angle $\theta = 0^\circ$, where the laser power density is range between 26 and 50 mW cm^{-2} . It is seen that the deflection angle increases from 0° to 60° as the laser power density increases from 26 to 43 mW cm^{-2} , where

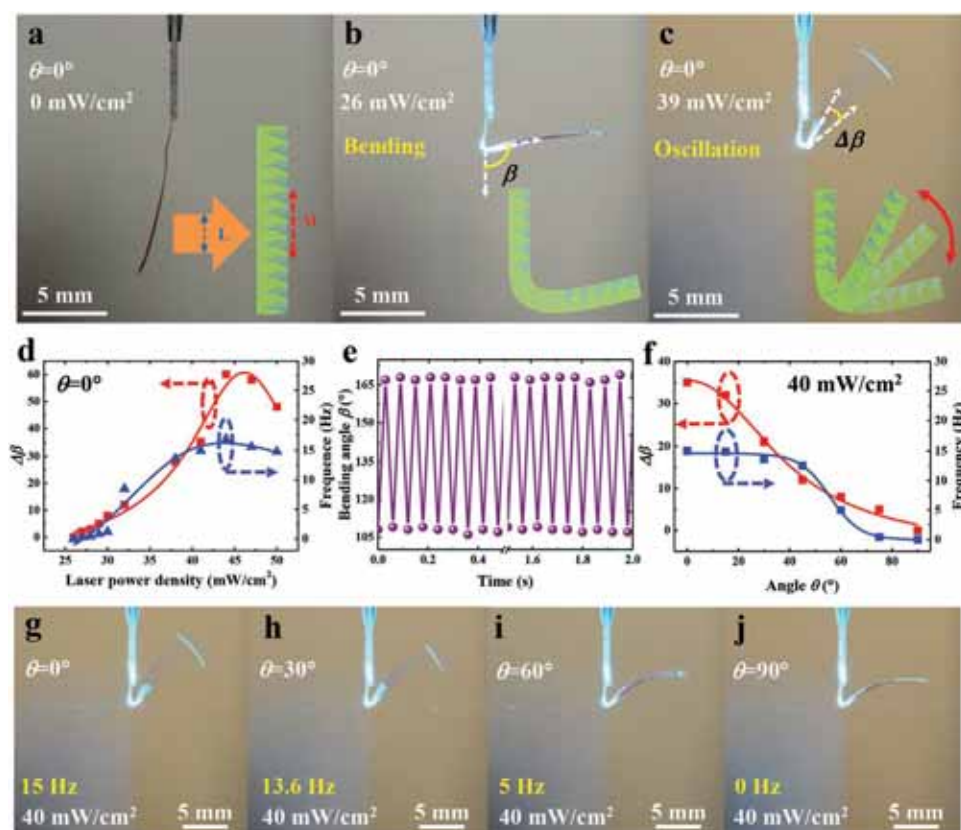


Figure 3. Polarization dependent LCE oscillators. a) Photo of LCE film actuator without light irradiation at $\theta = 0^\circ$. b) Photo of LCE film actuator at laser power density of 26 mW cm^{-2} and $\theta = 0^\circ$, where laser power density is the threshold for oscillation and the film demonstrates bending. c) Photo of LCE film oscillator at 39 mW cm^{-2} and $\theta = 0^\circ$, where the film oscillates at 14.9 Hz . The cross sectional schematic illustration of LCE film is demonstrated in (a)–(c). d) The deflection angle $\Delta\beta$ (red curve) and oscillation frequency (blue curve) as function on laser power density at angle $\theta = 0^\circ$. e) Plot of the bending angle versus time during exposure in laser power density of 43 mW cm^{-2} and $\theta = 0^\circ$. f) The deflection angle $\Delta\beta$ (red curve) and oscillation frequency (blue curve) as function on angle θ in range between 0° and 90° , where the laser power density is fixed at 40 mW cm^{-2} . The series of snapshots extracted from the video depicting film oscillations at fixed laser power density of 40 mW cm^{-2} for different θ of g) 0° , h) 30° , i) 60° , and j) 90° .

the corresponding oscillation frequency increases from 0 to 16.7 Hz . In contrast, the deflection angle and oscillation frequency decreases when the laser power density continues to increase larger than 43 mW cm^{-2} . The LCE oscillator tuning by different laser power density at $\theta = 0^\circ$ is shown in Video S3 in the Supporting Information. Figure 3e shows the bending angle versus time in laser power density of 43 mW cm^{-2} and $\theta = 0^\circ$. The LCE film demonstrated a fully reversible and continuous actuation with deflection angle of 60° and frequency of 16.7 Hz , where the bending angle was in range between 106° and 166° .

It can be seen that the local temperature of the LCE is mainly determined by the laser power density and the angle θ . Besides laser power density, the polarization (θ) is an additional controlling parameter that can be used for actuator tuning in our experiment. Figure 3f plots the deflection angle $\Delta\beta$ (red curve) and oscillation frequency (blue curve) as function on angle θ in range between 0° and 90° , where the laser power density is fixed at 40 mW cm^{-2} . Both of the deflection angle and oscillation frequency decrease as the θ increases from 0° to 90° , where the deflection angle $\Delta\beta$ drops from 35° to 0° and the oscillation frequency drops from 15 to 0 Hz . These results indicate that the oscillator can be modulated by not only light power density

but also the polarization direction of light. Figure 3g–j shows the series of snapshots extracted from the video (Video S4, Supporting Information) depicting film oscillations at fixed laser power density of 40 mW cm^{-2} for different θ of 0° , 30° , 60° , and 90° , which corresponds to oscillation frequency of 15 , 13.6 , 5 , and 0 Hz , respectively. Therefore, the polarization of light is a useful way for tuning the light-driven oscillator based on photo-thermal effect. The long-term stability of the oscillator is investigated and the relationship of illumination time and bending angle of the oscillator is shown in Figure S5 in the Supporting Information. The deflection angle ($\Delta\beta$) was collected at 10 min interval for 2 h (the maximum continuous working time of our laser), showing a good long-term stability of the oscillator.

Another LCE film (Sample 2) with size of $0.2 \text{ cm} \times 2 \text{ cm}$ was cut from the prepared film as bionic dog swinging tail. The alignment direction of RMs on the PA surface (M) was 45° to the long and short side of the rectangle LCE film, as shown in Figure 4a. Herein, the polarization direction of laser, irradiating from bottom to up, was parallel to the alignment direction of the RMs on PA surface ($L//M$). When light is on, the film will bend along M direction first and then swing back toward its original position, leading to a reversible swinging as a bionic dog tail. Figure 4b–g shows the series of snapshots extracted

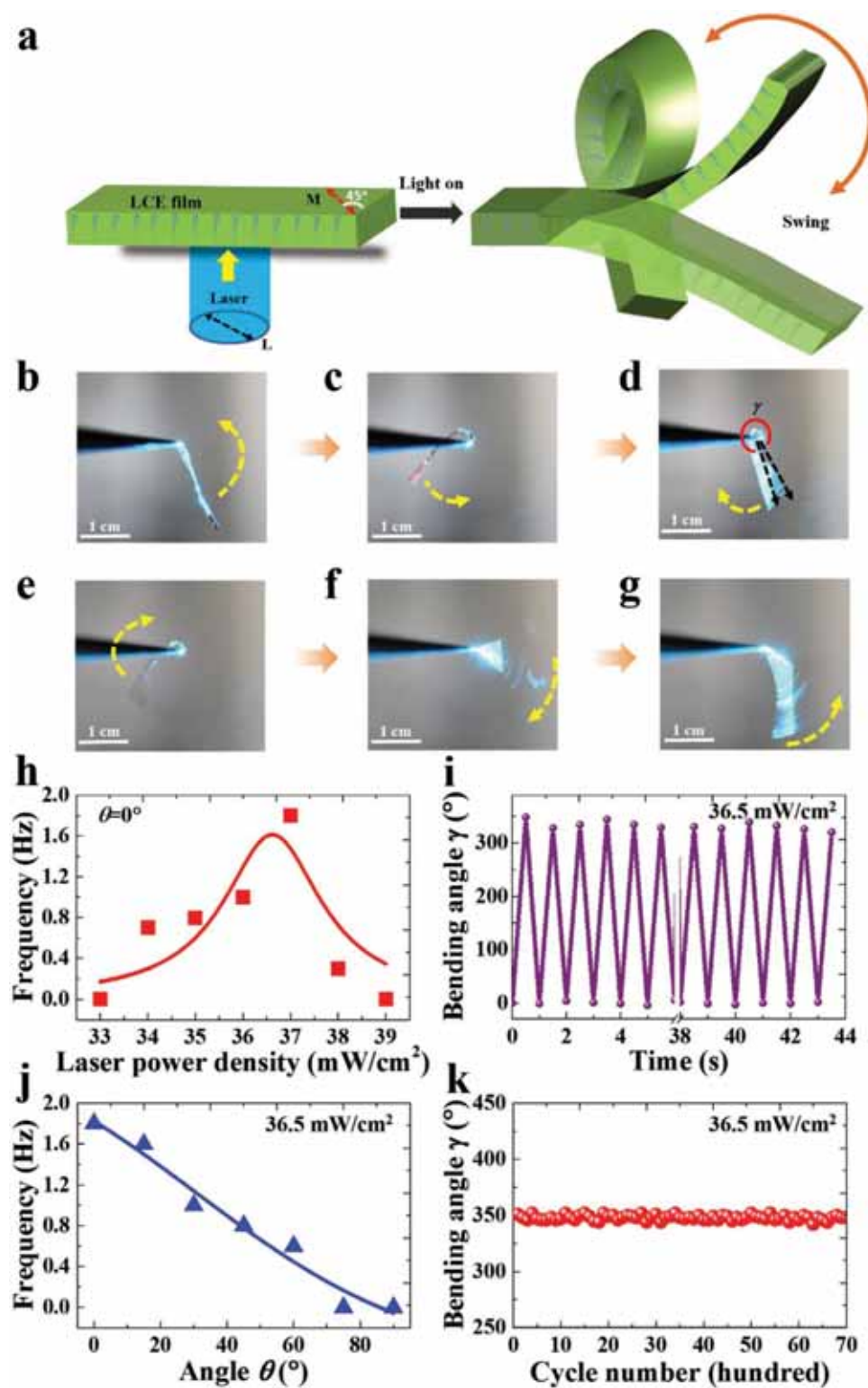


Figure 4. LCE based bionic dog swinging tail. a) Schematic diagrams of the bionic dog swinging tail based on DD-doped LCE. The alignment direction of RMs on the PA surface (M) is 45° to the long and short side of the rectangle LCE film. b–g) The series of snapshots extracted from the video depicting film swinging at fixed laser power density of 36.5 mW cm^{-2} . h) The swinging frequency as a function of laser power density at $\theta = 0^\circ$. i) The relationship of bending angle (γ) and illumination time when exposed to laser density of 36.5 mW cm^{-2} with $\theta = 0^\circ$, where the tail swinging angle is around 350° and the swinging frequency is 1 Hz. j) The swinging frequency as a function of angle θ at laser power density of 36.5 mW cm^{-2} . k) Repeatable actuation of the DD-doped LCE actuator under test of 7000 cycles.

from the video (Video S5, Supporting Information) depicting film swinging at fixed laser power density of 36.5 mW cm^{-2} . The swinging can be divided to two stages. In the first stage of bending (increase of bending angle), the LCE film swinging tail was demonstrated as the initial position (Figure 4b), middle state position (Figure 4c), and ending position (Figure 4d) as light was on. In Figure 4b, the LCE film prolapsed to the gravity of itself. The bending angle increases gradually when increasing the laser power density and the film bends and spans the tweezers as shown in Figure 4c,d. In Figure 4d, the maximal bending angle (or swinging angle) of the swinging tail is represented by γ (350° in this case) that is the angle between the initial and ending position of bending. As the increase of bending angle, the absorption ability of DD became weaker due to the increased angle between the alignment direction of DD and the polarization direction of laser. At the same time, the bending behavior of the film made some part of film out of irradiation area, resulting in reduce of the laser illumination region. Therefore, both the bending angle and the temperature of swinging tail would decrease when the LCE film bent to its ending position.

In the second stage of retrieving (decrease of bending angle), the LCE film swinging tail returned to its original position, as shown in Figure 4e–g. Both the bending angle and the temperature of swinging tail would increase again when the LCE film returned back to its original position. Based on these two processes mentioned above, both of the temperature of LCE film and the bending angle first increased and then reduced, leading to a reversible swinging action as bionic dog tail. It is noticed that the laser power density threshold of swinging was 33 mW cm^{-2} in our experiment. The bending direction in Figure 4b–g is represented by the yellow arrow.

The swinging frequency as a function of laser power density at $\theta = 0^\circ$ is plotted in Figure 4h. The swinging frequency increases from 0 to 1.8 Hz as increasing the laser power density from 33 to 37 mW cm^{-2} and decreases from 1.8 to 0 Hz as decreasing the laser power density from 37 to 39 mW cm^{-2} , which is due to decrease of absorption of DD as bending angle increases. The large laser power density leads to consistently increase of temperature of film, where the LC mesogens cannot be reoriented to LC phase thus no swinging action. Figure 4i shows the relationship of bending angle (γ) and illumination time when exposed to laser density of 36.5 mW cm^{-2} with $\theta = 0^\circ$, where the tail swinging angle is around 350° and the swinging frequency is 1 Hz. As expected, the polarization direction of light plays an important role of tuning swinging frequency while changing the angle θ . The swinging frequency as a function of angle θ is demonstrated in Figure 4j, where the laser power density is 36.5 mW cm^{-2} . It can be seen that the swinging frequency is tunable as the change of angle θ . The swinging frequency decreases gradually from 1.8 to 0 Hz with increase of angle θ from 0° to 90° . The repeatable actuation of the DD-doped LCE actuator under test of 7000 cycles is shown in Figure 4k, without obviously degradation during exposure of laser with power density 43 mW cm^{-2} and $\theta = 0^\circ$. The value of γ is around 350° here. The corresponding video for swinging tail tuning at different polarization direction of light is shown in Video S6 in the Supporting Information.

In addition, an application of the proposed linearly polarized light-driven actuators based on DD-doped LCE, a light-mill, is proposed and demonstrated in Figure 5. The schematic illustration of light-mill is demonstrated in Figure 5a. It is seen that the light-mill is consisted of a microtubule with internal diameter of $200 \text{ }\mu\text{m}$, four polyethylene glycol terephthalate (PET) holders with length of 2 cm, and four LCE films with size of $1 \text{ cm} \times 1.5 \text{ cm}$ (Sample 3) as four leaves of the light-mill, where the alignment direction of RMs on the PA surface (M) is parallel to the longer side, and the shorter side of LCE is sealed on the PET holder with epoxy resin. The optical setup of light-mill consists of a laser with wavelength of 488 nm, a polarizer, and a half-wave plate for polarization control. In order to have enough optical power density to bend the LCE film, only one of the four leaves is driven by linearly polarized light (L). At the beginning, the polarization direction of light is parallel to the alignment direction of RMs on the PA surface ($L//M$), the bending of the leaves causes the air to flow and generate an force along the bending direction, and the flow of air in turn generates a repeal force (F) on the leaves with opposite direction to the bending direction. Under light illumination, the generated power of light-mill can be estimated by $P = \eta \cdot 1/2 \cdot \rho \cdot v^3 \cdot S$, where η is light-mill efficiency, ρ is the density of air, v is the speed of air flow, and the S is area of leaf. The larger light power density leads to faster bending of leaf and bigger air flow, which finally leads to faster rotation of light-mill. Therefore, the speed of light-mill, which is highly related to the speed of air flow, is determined by the power density of the driven light source. In addition, the mass center of the whole light-mill will be shifted, resulting in a torque for the light-mill. The torque can be expressed as $T = mg\Delta L$, where the m is mass of the windmill, g is acceleration of gravity, and ΔL is shift length of mass center. Then the light-mill rotates under the joint action of the reaction force and torque rising from the bending leaves.

Figure 5b–e shows the series of snapshots extracted from the video (Video S7, Supporting Information) depicting light-driven rotation of light-mill at laser power density of 120 mW cm^{-2} . Figure 5f depicts the rotation speed of light-mill as function on the laser power density at wavelength of 488 nm. It can be seen that the rotation speed of light-mill increases from 0 to 30 rmp as the laser power density increases from 100 to 150 mW cm^{-2} . Here, the laser power density threshold for rotation is 100 mW cm^{-2} . Similar to the oscillator and swinging tail, the light-mill can be modulated by not only light power density but also the polarization direction of light. Figure 5g shows the relationship of rotation speed and angle θ at fixed laser power density of 150 mW cm^{-2} and wavelength of 488 nm. It can be seen that, when the angle θ increases from 0° to 90° , the rotation speed of light-mill decreases from 30 to 0 rmp, indicating that the light-mill motion can be modulated by polarization direction of light (Video S8, Supporting Information). To the best of our knowledge, the polarization-dependent LCE light-mill based on photothermal effect is experimentally demonstrated for the first time.

In summary, we demonstrate linearly polarized light-driven soft actuators based on DD doped LCE, which show excellent linearly polarization-dependent response under illumination of visible light 488 nm. Three LCE actuators,

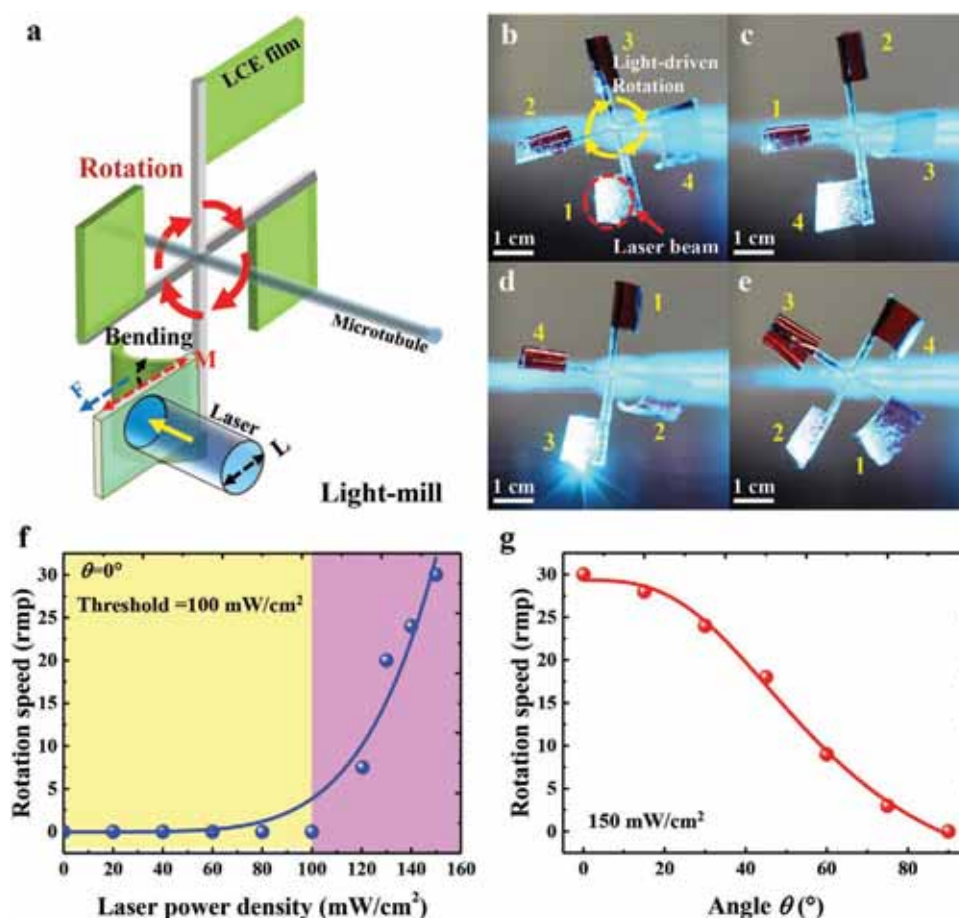


Figure 5. Polarization dependent LCE light-mill. a) schematic illustration of light-mill based on LCE films. b–e) The series of snapshots extracted from the video depicting light-driven rotation of light-mill at laser power density of 120 mW cm⁻². f) Rotation speed of light-mill as function on the laser power density at wavelength of 488 nm. The laser power density threshold for rotation is 100 mW cm⁻². c) Relationship of rotation speed and angle θ at fixed laser power density of 150 mW cm⁻² and wavelength of 488 nm.

including oscillators, bionic dog swinging tail, and light-mill are fabricated and investigated, where the polarization is used as a controlling parameter for actuator tuning. The polarization-dependent LCE oscillator demonstrates a fully reversible and continuous actuation with deflection angle of 60° and frequency of 16.7 Hz under laser power density of 43 mW cm⁻². In addition, a polarization-dependent bionic dog swinging tail is prepared by LCE with alignment direction of RMs on PA surface of LCE is 45° to the long and short side of the rectangle LCE film. The frequency of the swinging tail can be tuned between 0 and 1.8 Hz while the polarization angle θ changes from 0° to 90°. Finally, a polarization-dependent LCE light-mill is proposed, which is capable of rotating at speed of 30 rpm at laser power density of 150 mW cm⁻² and speed is tunable between 0 and 30 rpm with the change of polarization of light. Thus, the polarization of light is experimentally demonstrated to perform controlling parameter and provide an additional DOF to photothermal effect based light-driven LCE actuators besides the wavelength and intensity of light, which is useful for broad applications prospects in robotic and biomimetic technology.

Experimental Section

Materials: In our experiment, the light-driven actuator consisted of RMs, DD (RL002, with absorption peak of 488 nm, from HCCH), and photoinitiator (Irgacure 651, from BASF). The RMs were formed by mixing RM257, and RM006 (all from Shijiazhuang Sdyano Fine Chemical, $n_{\text{ave}} = 1.58$). The weight ratio of RM257, RM006, RL002, and Irgacure 651 was 36: 60.5: 1.5: 2. The chemical structures of the RM monomers are shown in Figure 1a.

Fabrication of LCE Film: Figure S1 (Supporting Information) depicts the fabrication process of proposed linearly polarized light-driven actuators based on DD-doped LCE. (i) First, the polyimide used for vertical or parallel alignment is coated on the indium tin oxide (ITO) coated glass by spin coating and then annealed. (ii) Then the vertical alignment (VA) or parallel alignment (PA) is achieved through rubbing the polyimide layer with a flannel in the selected direction. (iii) After that, the RM mixture (with DD and photoinitiator) was sandwiched in a cell, which was assembled by two pieces of oriented substrates with VA and PV alignment, respectively. The thickness of the LC cell was 45 μm . (iv) The LC cell was exposed under UV light (central wavelength at 365 nm) for 1 h at intensity of 4 mW cm⁻² to make the RM align well. (v) Finally, the free standing LCE film was obtained by removing glass substrates. The cross-section image obtained by scanning electron microscope (SEM) is shown in the Figure S6 (Supporting Information), where the thickness of LCE was measured to be around 45 μm .

Physical Parameters Measured: The setup for transmittance measurement consisted of a laser with wavelength of 488 nm and a power meter. The transmittance can be calculated according to $T = P_1/P_0$, where the P_1 is the power of the laser after passing through the sample, and the P_0 is the power of the laser without sample. The absorption of DD was measured by UV-vis spectrophotometer (Shanghai Yuanxi Co., Ltd.). The temperature of the LCE film was measured by thermal imager (FLIR One). The bending angle was measured by a protractor. The setup for frequency recording consisted of an oscilloscope, a laser with wavelength of 532 nm, and photoelectric probe. LCE films with a thickness of about 45 μm were measured to show a breakdown strength of 2.49 MPa at a strain of 0.9% in a tensile test (Figure S7, Supporting Information), manifesting fairly good mechanical properties.

Supporting Information

Supporting Information is available from the Wiley Online Library or from the author.

Acknowledgements

This work was supported by Natural National Science Foundation of China (NSFC) (61875081); Shenzhen Science and Technology Innovation Council (JCYJ20180305180700747).

Conflict of Interest

The authors declare no conflict of interest.

Keywords

actuators, light-driven, liquid crystal elastomers, soft robotics

Received: October 28, 2020

Revised: December 6, 2020

Published online: December 18, 2020

- [1] a) H. Yuk, S. Lin, C. Ma, M. Takaffoli, N. X. Fang, X. H. Zhao, *Nat. Commun.* **2017**, *8*, 14230; b) A. Miriyev, K. Stack, H. Lipson, *Nat. Commun.* **2017**, *8*, 596; c) W. Q. Hu, G. Z. Lum, M. Mastranglei, M. Sitti, *Nature* **2018**, *554*, 81; d) J. M. McCracken, B. R. Donovan, T. J. White, *Adv. Mater.* **2020**, *32*, 1906564.
- [2] a) R. Yang, Y. Zhao, *Angew. Chem., Int. Ed.* **2017**, *56*, 14202; b) J. A. Lv, Y. Y. Liu, J. Wei, E. Q. Chen, L. Qin, Y. L. Yu, *Nature* **2016**, *537*, 179; c) L. Hines, K. Petersen, M. Sitti, *Adv. Mater.* **2016**, *28*, 3690; d) J. Li, X. Zhou, Z. Liu, *Adv. Opt. Mater.* **2020**, *8*, 2000886.
- [3] a) T. J. White, D. J. Broer, *Nat. Mater.* **2015**, *14*, 1087; b) H. Zeng, P. Wasylczyk, D. S. Wiersma, A. Priimagi, *Adv. Mater.* **2018**, *30*, 1703554; c) Z. C. Jiang, Y. Y. Xiao, Y. Zhao, *Adv. Opt. Mater.* **2019**, *7*, 1900262; d) G. Stoychev, A. Kirillova, L. Ionov, *Adv. Opt. Mater.* **2019**, *7*, 1900067; e) Y. Shang, J. Wang, T. Ikeda, L. Jiang, *J. Mater. Chem. C* **2019**, *7*, 3413.
- [4] a) T. Ikeda, J. Mamiya, Y. Yu, *Angew. Chem., Int. Ed.* **2007**, *46*, 506; b) T. Ube, T. Ikeda, *Adv. Opt. Mater.* **2019**, *7*, 1900380; c) M. Yamada, M. Kondo, J. Mamiya, Y. Yu, M. Kinoshita, C. J. Barrett, T. Ikeda, *Angew. Chem., Int. Ed.* **2008**, *47*, 4986; d) M. Wang, B. P. Lin, H. Yang, *Nat. Commun.* **2016**, *7*, 13981; e) A. H. Gelebart, D. J. Mulder, M. Varga, A. Konya, G. Vantomme, E. W. Meijer, R. L. B. Selinger, D. J. Broer, *Nature* **2017**, *546*, 632; f) X. Lu, S. Guo, X. Tong, H. Xia, Y. Zhao, *Adv. Mater.* **2017**, *29*, 1606467; g) X. Pang, J. Lv, C. Zhu, L. Qin, Y. Yu, *Adv. Mater.* **2019**, *31*, 1904224; h) M. Baroncini, S. Silvi, A. Credi, *Chem. Rev.* **2020**, *120*, 200; i) F. Ge, Y. Zhao, *Adv. Funct. Mater.* **2020**, *30*, 1901890.
- [5] L. Dong, Y. Zhao, *Mater. Chem. Front.* **2018**, *2*, 1932.
- [6] a) L. Yang, K. Setyowati, A. Li, S. Gong, J. Chen, *Adv. Mater.* **2008**, *20*, 2271; b) R. R. Kohlmeyer, J. Chen, *Angew. Chem., Int. Ed.* **2013**, *52*, 9234; c) H. Kim, J. A. Lee, C. P. Ambulo, H. B. S. Lee, H. Kim, V. V. Naik, C. S. Haines, A. E. Aliev, R. O. Robles, R. H. Baughman, T. H. Ware, *Adv. Funct. Mater.* **2019**, *29*, 1905063; d) M. Wang, S. M. Sayed, L. X. Guo, B. P. Lin, X. Q. Zhang, Y. Sun, H. Yang, *Macromolecules* **2016**, *49*, 663; e) C. Li, Y. Liu, X. Huang, H. Jiang, *Adv. Funct. Mater.* **2012**, *22*, 5166; f) Y. Yang, Z. Pei, Z. Li, Y. Wei, Y. Ji, *J. Am. Chem. Soc.* **2016**, *138*, 2118; g) J. Li, L. Mou, R. Zhang, J. Sun, R. Wang, B. An, H. Chen, K. Inoue, R. O. Robles, Z. Liu, *Carbon* **2019**, *148*, 487; h) T. Wang, D. Torres, F. E. Fernández, C. Wang, N. Sepúlveda, *Sci. Adv.* **2017**, *3*, e1602697.
- [7] a) X. Liu, R. Wei, P. T. Hoang, X. Wang, T. Liu, P. Keller, *Adv. Funct. Mater.* **2015**, *25*, 3022; b) X. Lu, H. Zhang, G. Fei, B. Yu, X. Tong, H. Xia, Y. Zhao, *Adv. Mater.* **2018**, *30*, 1706597; c) Z. Wu, L. Liu, P. Cheng, J. Fang, T. Xu, D. Chen, *J. Mater. Chem. C* **2019**, *7*, 14245.
- [8] a) L. Yu, Z. Cheng, Z. Dong, Y. Zhang, H. Yu, *J. Mater. Chem. C* **2014**, *2*, 8501; b) Z. Cheng, T. Wang, X. Li, Y. Zhang, H. Yu, *ACS Appl. Mater. Interfaces* **2015**, *7*, 27494; c) W. Wei, Z. Zhang, J. Wei, X. Li, J. Guo, *Adv. Opt. Mater.* **2018**, *6*, 1800131.
- [9] a) L. T. de Haan, C. S. Somolinos, C. M. W. Bastiaansen, A. P. H. J. Schenning, D. J. Broer, *Angew. Chem., Int. Ed.* **2012**, *51*, 12469; b) L. Liu, M. H. Liu, L. L. Deng, B. P. Lin, H. Yang, *J. Am. Chem. Soc.* **2017**, *139*, 11333; c) M. Lahikainen, H. Zeng, A. Priimagi, *Nat. Commun.* **2018**, *9*, 4148; d) A. H. Gelebart, G. Vantomme, E. W. Meijer, D. J. Broer, *Adv. Mater.* **2017**, *29*, 1606712; e) O. M. Wani, H. Zeng, A. Priimagi, *Nat. Commun.* **2017**, *8*, 15546; f) M. Rogó, H. Zeng, C. Xuan, D. S. Wiersma, P. Wasylczyk, *Adv. Opt. Mater.* **2016**, *4*, 1689; g) H. Zeng, O. M. Wani, P. Wasylczyk, A. Priimagi, *Macromol. Rapid Commun.* **2018**, *39*, 1700224; h) F. Ge, R. Yang, X. Tong, F. Camerel, Y. Zhao, *Angew. Chem., Int. Ed.* **2018**, *57*, 11758; i) S. Palagi, A. G. Mark, S. Y. Reigh, K. Melde, T. Qiu, H. Zeng, C. Parmeggiani, D. Martella, A. S. Castillo, N. Kapernaum, F. Giesselmann, D. S. Wiersma, E. Lauga, P. Fischer, *Nat. Mater.* **2016**, *15*, 647; j) H. Zeng, H. Zhang, O. Ikkala, A. Priimagi, *Matter* **2020**, *2*, 194; k) J. Li, R. Zhang, L. Mou, M. J. de Andrade, X. Hu, K. Yu, J. Sun, T. Jia, Y. Dou, H. Chen, S. Fang, D. Qian, Z. Liu, *Adv. Funct. Mater.* **2019**, *29*, 1808995.
- [10] a) W. Liu, L. X. Guo, B. P. Lin, X. Q. Zhang, Y. Sun, H. Yang, *Macromolecules* **2016**, *49*, 4023; b) H. Tian, Z. Wang, Y. Chen, J. Shao, T. Gao, S. Cai, *ACS Appl. Mater. Interfaces* **2018**, *10*, 8307; c) J. R. Sun Lan, C. Shen, R. Huang, Z. Zhang, L. Zhang, L. Wang, H. Yang, *Adv. Mater.* **2020**, *32*, 1906319.
- [11] B. Zuo, M. Wang, B. P. Lin, H. Yang, *Nat. Commun.* **2019**, *10*, 4539.
- [12] L. Dong, X. Tong, H. Zhang, M. Chen, Y. Zhao, *Mater. Chem. Front.* **2018**, *2*, 1383.